PHYSICAL REVIEW E **86**, 061317 (2012)

Effect of confinement on dense packings of rigid frictionless spheres and polyhedra

Jean-François Camenen,[1,*] Yannick Descantes,[1,†] and Patrick Richard[1,2,‡]
[1]*LUNAM Université, IFSTTAR, site de Nantes, Route de Bouaye CS4, 44344 Bouguenais Cedex, France*
[2]*Institut Physique de Rennes, Université de Rennes I, UMR CNRS 6251, 35042 Rennes, France*

(Received 11 May 2012; revised manuscript received 26 October 2012; published 26 December 2012)

We study numerically the influence of confinement on the solid fraction and on the structure of three-dimensional random close-packed granular materials subject to gravity. The effects of grain shape (spherical or polyhedral), material polydispersity, and confining wall friction on this dependence are investigated. In agreement with a simple geometrical model, the solid fraction is found to decrease linearly for increasing confinement no matter the grain shape. Furthermore, this decrease remains valid for bidisperse sphere packings, although the gradient seems to reduce significantly when the proportion of small particles reaches 40% by volume. The confinement effect on the coordination number is also captured by an extension of the aforementioned model.

DOI: 10.1103/PhysRevE.86.061317 PACS number(s): 45.70.Cc, 61.43.−j

I. INTRODUCTION

Granular materials are well known for their wide range of fascinating properties. Their theoretical description is difficult for many reasons. One of them is the importance of the local arrangement of grains within the material on its macroscopic behavior. Real granular systems have boundaries, but for the sake of simplicity, scientists often neglect them (see, for example, Refs. [1,2]) and the system is then considered as infinite. This assumption is not always justified since the presence of boundaries modifies the system local arrangement in their vicinity. Moreover, due to the intrinsic steric hindrance of granular materials, those structure modifications often propagate over distances in the order of several grain sizes. As a consequence, the behavior of granular systems may be strongly influenced by the presence of sidewalls even if the confinement length is large compared to the grain size.

The crucial role of confinement on system properties has been pointed out in many works dealing with gravity-driven granular flows [3–8], granular segregation [9], structure and mechanics of granular packings [10–12], granular systems in narrow silos [13], or granular penetration by impact [14]. Those studies point out that two major physical properties can be influenced by the presence of sidewalls. First, they can induce friction that might be important in respect to the internal friction of the system [7], explaining the well-known Janssen effect [15], or unexpectedly high angle values observed with confined granular heaps [16,17] or confined chute flows [3]. Second, as mentioned above, they might also alter the geometrical structure of the system near the wall, where particles tend to form layers, giving rise to a fluctuating local solid fraction with distance from the wall [11] and affecting the properties of confined systems. Note that the effect of confinement is not limited to the vicinity of the walls but may propagate within the sample. This is more particularly the case for confined granular chute flows for which it has been shown that the good dimensionless number to quantify the sidewall effect is not the number of grains per unit of width between sidewalls but the ratio of the flow height to the gap between sidewalls [3].

Here, we focus mainly on the geometric effect of the presence of sidewalls on quantities like the solid fraction and the coordination numbers. Recently, Desmond and Weeks used numerical simulations to study the effect of confinement on binary atomic systems at the random-close-packing limit [18]. Their numerical results agree with a simple geometrical model [19–21] (hereafter called the geometrical model), which captures the evolution of the solid fraction of random close packings of spheres with confinement. It is based on the following configuration: A packing of particles is confined between two parallel and flat walls separated by a gap W. It then assumes that such a confined system is made of two boundary layers (of thickness h) and a bulk region and that the solid fraction of the boundary layers, ϕ_{BL}, is lower than that of the bulk region, ϕ_{bulk}. By writing the total solid fraction ϕ as the average of both the bulk region and boundary layers' solid fractions (weighted by their relative thickness), the geometrical model predicts that the average solid fraction decreases linearly with $1/W$,

$$\phi = \frac{W-2h}{W}\phi_{\mathrm{bulk}} + \frac{2h}{W}\phi_{\mathrm{BL}} = \phi_{\mathrm{bulk}} - \frac{C}{W}, \qquad (1)$$

where $C = 2h\,(\phi_{\mathrm{bulk}} - \phi_{\mathrm{BL}})$. Note that this model can be easily adapted to other boundaries, such as cylindrical ones [18]. The three parameters of the geometrical model (ϕ_{bulk}, ϕ_{BL}, and h) probably depend on grain shape, packing polydispersity, and confining wall properties. Here we study the effect of confinement on quasistatic dense frictionless granular systems (i.e., grains interacting through hard core repulsion) subjected to gravity. We test the validity of the geometrical model for such systems and study the aforementioned dependencies. Using numerical simulations, we investigate the actual effect of grain shape by comparing packings of spheres with packings of polyhedra. Furthermore, we assess the effect of packing polydispersity by comparing monosized and binary packings. In addition, we check the effect of grain-wall friction. Eventually, we look into packing microstructure by studying the effect of confinement on the coordination number.

The paper is organized as follows. Section II describes our simulations with details as well as the numerical simulation method used. After checking the state of packings in Sec. III,

---

[*] jfcamenen@gmail.com

[†] yannick.descantes@ifsttar.fr

[‡] patrick.richard@ifsttar.fr

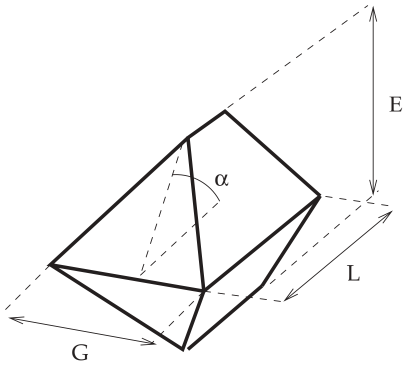

FIG. 1. Pinacoid, a model polyhedra characterized by its length L, width G, height E, and angle α.

Sec. IV investigates how the solid fraction is modified by confinement and how these modifications are influenced by packing polydispersity, grain shape, and confining wall friction. Then we examine in Sec. V the modification of the packing microstructure with confinement. Finally, in Sec. VI, we summarize our results and present our conclusions.

II. SIMULATION METHODOLOGY

A. Geometry of grains

The simulated system is a three-dimensional dense assembly of n frictionless rigid grains of mass density ρ, interacting with each other through totally inelastic collisions.

Since grain shape may influence the behavior of granular materials [22–25], two types of grains have been studied: spherical grains of average diameter d and polyhedra of average characteristic dimension d. The polyhedra shape (Fig. 1) is that of a *pinacoid*, with eight vertices, 14 edges, and eight faces. This polyhedron has three symmetry planes and is determined by four parameters: length L, width G, height E, and angle α. According to an extensive experimental study with various rock types reported by Ref. [26], the pinacoid gives the best fit among simple geometries for an aggregate grain. In order to have a similar aspect ratio for both grain shapes, the pinacoid dimensional parameters were taken to be identical ($L = G = E$), with the characteristic dimension d expressed as $d = L$. In addition, angle α was set to 60°. For each grain shape, two grain diameters (or characteristic dimensions) have been considered: large d_L and small $d_S = d_L/2$.

B. Samples preparation

The packing geometry is that of a parallelepiped (Fig. 2) of dimensions L_x by L_y by L_z. Periodic boundary conditions (PBC) are applied in the x direction to simulate an infinitely long parallelepiped using a finite number of grains. The packing is confined in the y direction between two fixed parallel walls separated from each other by a $L_y = W$ large gap. In some cases, PBC are also applied along the y axis to simulate unconfined reference state, with W set to $20d_L$. The packing is supported on the xy plane by a fixed frictionless bottom wall and delimited by a free surface at its top.

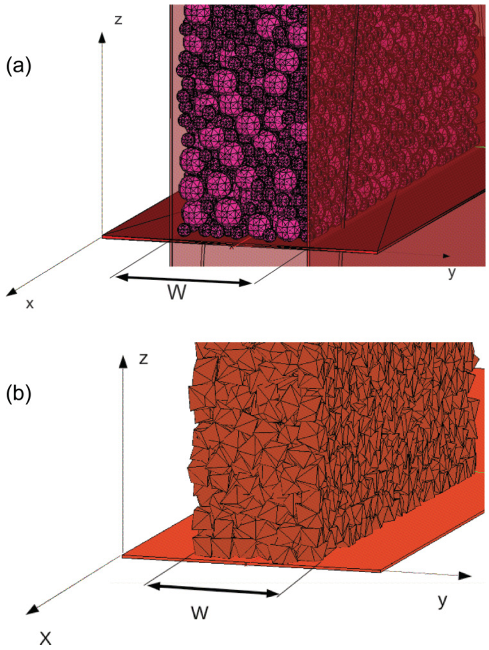

FIG. 2. (Color online) Typical 3D snapshots of packings made of polysized spheres (a) and pinacoids (b). The confinement is characterized by the gap W between sidewalls. The direction of gravity is $-z$.

Grain samples are composed of various proportions of small and large grains having the same shape. In order to reduce the thickness of the crystallized layer commonly observed inside confined packings at the interface with smooth walls [27,28], each population of grain size is randomly generated with a Gaussian distribution characterized by its mean d and its variance $d^2/900$. For the sake of simplicity, packings made of a unique population of grains (either small or large) will be called "monodisperse," whereas packings made of small and large grains will be called "bidisperse" in the following. In the latter case, the proportions of small (x_S) and large (x_L) grains expressed as percentages by volume are of course linked through $x_S = 100 - x_L$.

Each sample is constructed layer by layer according to the following geometrical deposition protocol inspired by Ref. [29]: Spherical particles of a sufficient diameter to circumscribe the larger grains of the sample are sequentially dropped along z in a parallelepiped box having the aforementioned geometry. Each particle stops on the free surface made of the underneath layer of particles (or on the bottom wall for the first layer of particles) and is further moved so it lays on three particles chosen to locally minimize its altitude z. Finally, the sample actual grains are randomly substituted for those spherical particles. For polyhedra samples, a random orientation is further assigned to each pinacoid. Note that according to this protocol, some of the deposited grains may not be in contact with their neighbors depending on their size and shape.

C. Initialization and solicitations

The system initialization is identical for spheres and pinacoids samples. The first step consists in geometrically depositing n grains into a parallelepiped box and then PBC are substituted for the lateral walls of the parallelepiped box along the x direction (along the x and y directions for biperiodic reference state). Finally, gravity $\vec{g}$ (0,0,$-g$) is applied in order to compact the sample.

D. Contact dynamics method

Discrete numerical simulations were performed using the contact dynamics (CD) method [30,31], which is specially convenient for rigid grains. This method is based on implicit time integration of the equations of motion with respect to generalized nonsmooth contact laws describing noninterpenetration and dry friction between grains. This formulation unifies the description of lasting contacts and collisions through the concept of impulse, which can be defined as the time integral of a force. The generalized nonsmooth contact laws are expressed in terms of impulse $\overrightarrow{P_C}$ and formal relative velocity $\overrightarrow{\overline{V}_C}$ at contact point C. If V_{CN}^-, V_{CT}^-, V_{CN}^+, and V_{CT}^+ denote the normal and tangential relative velocities at contact point respectively before and after collision, the formal normal and tangential relative velocities are defined as follows:

$$\bar{V}_{CN} = \frac{V_{CN}^+ + e_N V_{CN}^-}{1 + e_N}, \qquad \bar{V}_{CT} = \frac{V_{CT}^+ + e_T V_{CT}^-}{1 + e_T}, \tag{2}$$

where e_N and e_T measure the inelasticity of collisions and reduce to the normal and tangential restitution coefficients in the case of binary collisions.

These generalized contact laws support momentum propagation through contact networks inherent to dense assemblies of grains. For a given time step, impulses and velocities are determined according to an iterative process using a nonlinear Gauss-Seidel–like method [32]. In the case of large size packings of rigid grains, the CD method supports larger time steps, leading potentially to faster calculations than the molecular dynamic method, for which small time steps are needed.

The CD method was applied using the LMGC90© platform [33,34], which namely implements a 3D extension of a 2D contact detection algorithm described with details in Ref. [35]. Basically, contacts with a given grain are sought exclusively among its neighbors. When a neighbor is located closer to the grain than a threshold distance called *gap*, a 3D extension of the *shadow-overlap method* devised by Moreau [33,36] is applied. In the case of overlap between the grain shades, their contact plane is determined. Four contact situations may be encountered (Fig. 3): vertex-to-face or edge-to-edge, represented by a single point and called *simple*; edge-to-face, represented by two points and called *double*; and, finally, face-to-face, represented by three points and called *triple* (vertex-to-edge and vertex-to-vertex being very unlikely to happen). These situations allow identification of a contact plane and compute the contact impulse and velocity components at each contact point.

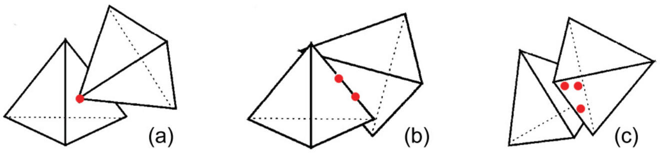

FIG. 3. (Color online) Two polyhedra can experience simple contacts (a), double contacts (b), or triple contacts (c).

This method proved apt to deal with dense flows of disks [37–39] as well as with quasi-static plastic deformation [35,40–44].

E. Materials and system parameters

The present study focuses on monodisperse sphere packings (MSP), bidisperse sphere packings (BSP), and monodisperse pinacoid packings (MPP).

The spacing of lateral walls W takes discrete values between $5d_L$ and $20d_L$, and the sample period along the x axis is $20d_L$. With the final height h of the packing in the range of $16d_L$ to $20d_L$, the number n of grains varies between 1900 and 30 400 for spheres, depending on the proportion by volume of small grains, and between 3600 and 15 000 for pinacoids.

The time-step value Δt is taken small enough to moderate the grain interpenetration incumbent to grains displacement between two successive implementations of the contact detection algorithm but sufficiently large to keep the calculation duration reasonable. In this perspective, limiting to $d_L/100$ the translation of grains during Δt seems appropriate. For our grain packings subject to compaction under their own weight, this leads to the following relation:

$$\frac{d_L}{100} = v_{\max}\Delta t, \tag{3}$$

with $v_{\max} = \sqrt{2g\Delta h}$ the maximum speed reached by a grain free falling from initial height of the deposited packing down to the altitude of the packing free surface at the end of the compaction. Hence, Eq. (3) leads to the following expression for the time step:

$$\Delta t = \frac{1}{100}\sqrt{\frac{d_L}{2\Delta h}}\sqrt{\frac{d_L}{g}}. \tag{4}$$

Although the between-grain friction is set to zero, that of wall-grain contacts (μ_w) is assigned nonzero values in a few simulations to study the influence of wall friction.

The simulated system parameters are summarized in Table I for spheres and in Table II for pinacoids. They are expressed as dimensionless quantities by defining the following normalization terms: lengths and times are respectively measured in units of d_L and $t_0 = \sqrt{d_L/g}$, the characteristic free fall time of a rigid grain of diameter d_L subject to gravity exclusively. For a given set of system parameters, three grain packings are simulated in order to average the various measured quantities.

TABLE I. Sphere packings.

n	x_s(%)	L_x/d_L	L_y/d_L	h/d_L	$\Delta t/\sqrt{d_L/g}$	μ_w	e_n,e_t
2300	0	20	5	16	3.10^{-4}	0.0	0.0
to	10		10	to	to	0.3	
30 400	25		20	20	10^{-3}	0.5	
	40					1.0	

TABLE II. Pinacoid packings.

n	L_x/d	L_y/d_L	h/d_L	$\Delta t/\sqrt{d_L/g}$	μ_w	e_n,e_t
3600	20	5	16	3.10^{-4}	0.0	0.0
to		10	to	to		
15 000		20	20	10^{-3}		

III. STATE OF PACKINGS

In order to examine the influence of wall-induced confinement on the solid fraction and structure of dense packings for various grain shape and polydispersity, it is necessary to adopt a reference packing state and to ensure that the compaction method used allows us to approximate such a state while providing sufficient repeatability for a given set of materials and system parameters. As mentioned in Sec. II C, the compaction method used consists in depositing rigid frictionless grains (with or without wall friction) under their own weight. For sphere packings with presumably negligible confinement, several authors have experimentally [45,46] or numerically [1,46,47] observed that this compaction method led to random close-packed states characterized by the generally agreed solid fraction value of 0.64. According to Ref. [48], random close-packed states of rigid frictionless grains (spherical or nonspherical) are equivalent to packing states in which the grains are homogeneously spread and in a stable equilibrium without crystallization or segregation (observe that the notion of "stable equilibrium" refers to the minimization of a potential energy that ensures maximum solid fraction [49]). Furthermore, extensive investigation of the random close-packed state carried out by the authors of Ref. [2] with spherical particles has evidenced the uniqueness of this state in the limit of infinitely large samples subject to fast isotropic compression (to avoid cristallization). Hence, the influence of wall-induced confinement on the solid fraction and structure of dense packings may be assessed against the random close-packed state taken as the reference. Keeping in mind that our compaction method allows us only to approximate the random close-packed state (our compression is not isotropic) and that the uniqueness of this reference state has only been evidenced for sphere packings, it is expected that meeting as much as possible the criteria stated by Ref. [48] will lead to sufficiently repeatable solid fraction and microstructure characteristics for a given set of materials and system parameters to observe confinement effects for various grain shapes and polydispersity. Therefore, preliminary assessment consists in checking the state of our simulated packings (both sphere and pinacoid packings) in terms of stable equilibrium, homogeneity, and reasonable interpenetration given the particularities of the contact dynamics method. Further assessment will be undertaken in Secs. IV and V.

A. Equilibrium

According to Ref. [2], grain packings for which the following criteria are met on each grain have reached a stable equilibrium,

$$\sum F < 10^{-4} d^2 P, \tag{5}$$

$$\sum M < 10^{-4} d^3 P, \tag{6}$$

$$E_c < 10^{-8} d^3 P, \tag{7}$$

where $\sum F$, $\sum M$, and E_c are, respectively, the net force, net momentum, and total kinetic energy of the grain. Indeed, the authors of Ref. [2] have observed that setting to zero all grain velocities in such a state and letting the packing relax further did not lead to any kinetic energy or unbalanced force level regain beyond these threshold values.

As a consequence, these criteria were used to check the attainment of a stable equilibrium state in our simulations, which was the case for all of them.

B. Interpenetration

The grain interpenetration, calculated as the sum of interpenetrated volumes between neighboring grains divided by the sum of grain volumes, was checked in the bulk region of the packing at the end of each simulation.

For sphere packings, the interpenetration was calculated analytically as the sum of interpenetrated volumes between couples of spheres (for a given couple of spheres, the interpenetrated zone consists of two spherical caps) and it was found to be very low (in the range of 10^{-5} to 10^{-3}% by volume).

For pinacoids, a routine was designed to compute the solid fraction as well as lower and upper bounds of the grain interpenetration. Basically, this routine consists of superimposing a lattice on the grain packing and calculating the solid volume in each cell of the lattice. For a given cell, this solid volume is the sum of elementary volumes analytically calculated from the intersection between any pinacoid and the cell. In order to bound the grain interpenetration, one shall focus on cells intersected by two neighboring pinacoids, leading to one of the four situations depicted on Fig. 4 (in 2D for simplicity reasons):

(i) In situations (a) and (b), the solid volume V_{sol} contained by the cell is in excess of actual cell volume V_{cell}; hence, the lower bound of actual interpenetrated volume is

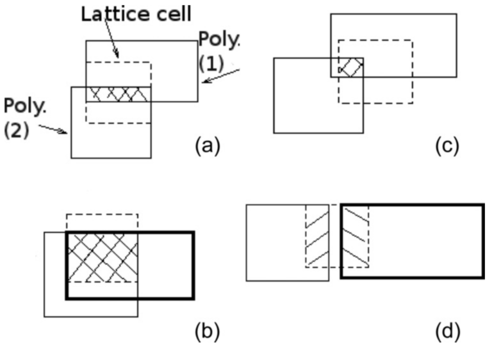

FIG. 4. 2D simplified representation of the four intersection situations between two pinacoids and a lattice cell: (a) solid volume ⩾ cell volume and partial interpenetration in the cell; (b) solid volume ⩾ cell volume and total interpenetration in the cell; (c) solid volume < cell volume and interpenetration (partial as represented or total); and (d) solid volume < cell volume and no interpenetration.

TABLE III. Pinacoid packings interpenetration for MPP.

W/d_L	5	10	20	PBC
$I_{\min}$ (% vol.)	4.6	4.5	3.4	3.5
$I_{\max}$ (% vol.)	5.0	4.7	3.6	3.7

$(V_{\mathrm{sol}} - V_{\mathrm{cell}})/2$ [situation (a)], whereas the upper bound is $V_{\mathrm{sol}}/2$ [situation (b)].

(ii) In situations (c) and (d), the solid volume contained by the cell is smaller than actual cell volume; hence, the lower bound of actual interpenetrated volume is 0 [situation (d)], whereas the upper bound is $V_{\mathrm{sol}}/2$ [situation (c)].

Observe that $V_{\mathrm{sol}}/2$ is the upper bound of the interpenetrated volume no matter the situation. When their size decrease, the lattice cells that are intersected by two pinacoids tend to concentrate exclusively inside actual interpenetrated areas (IA), where $V_{\mathrm{sol}}/2 = V_{\mathrm{cell}}$ or astride their border (AB), where $0 < V_{\mathrm{sol}}/2 < V_{\mathrm{cell}}$. Hence, the total interpenetrated volume of the packing V_I is bounded by the following interval:

$$V_I \in \left[\sum_{\mathrm{cell} \in IA} V_{\mathrm{cell}} \,;\, \sum_{\mathrm{cell} \in IA} V_{\mathrm{cell}} + \sum_{\mathrm{cell} \in AB} V_{\mathrm{cell}} \right],$$

in which $\sum_{\mathrm{cell} \in AB} V_{\mathrm{cell}}$ tends to zero with decreasing cell size.

For each pinacoid packing geometry, Table III gathers lower $I_{\min}$ and upper $I_{\max}$ bounds of grain interpenetration, e.g., bounds of V_I expressed as a percentage of the packing solid volume. These values were computed in the bulk region using a lattice with $d_L/20$ large cubical cells, and each of them was averaged over three simulations. The interpenetration calculated in our pinacoid packings, in the range of 3 to 5% by volume, is clearly much higher than the one calculated for sphere packings.

A first reason to explain these differences lies with the determination of contact between two grains. In the case of sphere packings, this determination is very simple and requires no interpenetration: grains are in contact when the distance between their centers is lower or equal to the sum of their radii. Such a contact is only one point, which is located on the segment connecting the centers of spheres at a distance of each sphere center equal to its radius. Besides, the orientation of the contact normal is borne by the segment connecting the grain centers. In the case of pinacoid packings, the determination of contact between two grains is much more complex and time-consuming and implies more or less interpenetration: first, grains are in contact when their respective shadows always overlap no matter the projection direction. Hence, much more calculation than for sphere packings shall be performed to prove the existence of a contact, and the simultaneous achievement of these overlap situations generally implies some interpenetration. Next, in the case of a contact, it may not be a unique point but rather two (edge-to-face contact) or three (face-to-face contact) points, as explained in Sec. II D, which obviously leads to more interpenetration.

A second reason lies with the nonsmooth approach associated with the contact dynamics. In molecular dynamics [50], contact forces increase proportionally to a power function of the interpenetration, leading to high repulsion contact forces and, thus, low interpenetration in the limit of rigid grains. In the contact dynamics method where no such relation is applicable, the interpenetration is namely monitored by the quality of the convergence of impulses and velocities at contact points within the range of permissible values on the generalized nonsmooth contact laws. Hence, in addition to an appropriate time-step value, a low level of interpenetration requires optimizing both the convergence criteria and number of Gauss-Seidel iterations while keeping the calculation time acceptable (for more information, refer to Refs. [30,31,33,34]).

Anyhow, the contact dynamics method is known to give interpenetration values in the order of a few percentages by volume (see Ref. [51]), and our quest of the densest possible disordered packing made of frictionless particles unsurprisingly leads to interpenetration values in the higher range. Hence, the interpenetration evidenced by our results is acceptable.

C. Homogeneity of distribution

In order to ensure that the applied compaction method leads to homogeneously distributed packings, we examine the variations in the proportions of large (P_L) and small (P_S) grains with distance z from the bottom wall [Figs. 5(a) and 5(b)]. Therefore, we count the number of particles of each size in d_L-thick regions of the packing and divide that number by the total number of grains. Although small deviations (that may be due to segregation) close to the bottom of our packings are observed, the proportion profiles are almost constant, showing that grains in sphere or pinacoid packings are reasonably vertically homogeneously distributed. The absence of segregation along the y axis is also checked for BSP in the homogeneous zone (e.g., far from bottom and free surface). Figure 5(c) displays the variations of proportions P_L and P_s in d_L-thick layers parallel to the sidewalls. The proportion profiles are almost constant, showing reasonable horizontal homogeneity.

IV. SOLID FRACTION

A. Average solid fraction

In this subsection, our aim is to study the effect of confinement on the solid fraction of MSP, BSP, and MPP, that is to say, for various proportions of small particles and various grain shapes. For this purpose, we report the evolution of the aforementioned quantity for several values of gap between sidewalls. We will also test the geometrical model mentioned in the introduction [cf. Eq. (1)]. The solid fraction is computed from analytical calculation of the volume of each sphere or each pinacoid present within a given volume. This volume incorporates any particle located $3d_L$ away from the bottom wall and the free surface. For the solid fraction of sphere packings, the use of the Voronoï tessellation [52,53] gives the same results.

Figure 6 reports the average solid fraction for BSP, MSP, and MPP versus d_L/W. A first observation is that for a fixed d_L/W value, an addition of small grains in a monosized sphere packing increases the solid fraction. This well-known phenomenon can easily be understood by considering two limit cases. The first one consists of a monosized sphere packing to which we add a few small particles ($x_s \ll 100\%$). In this

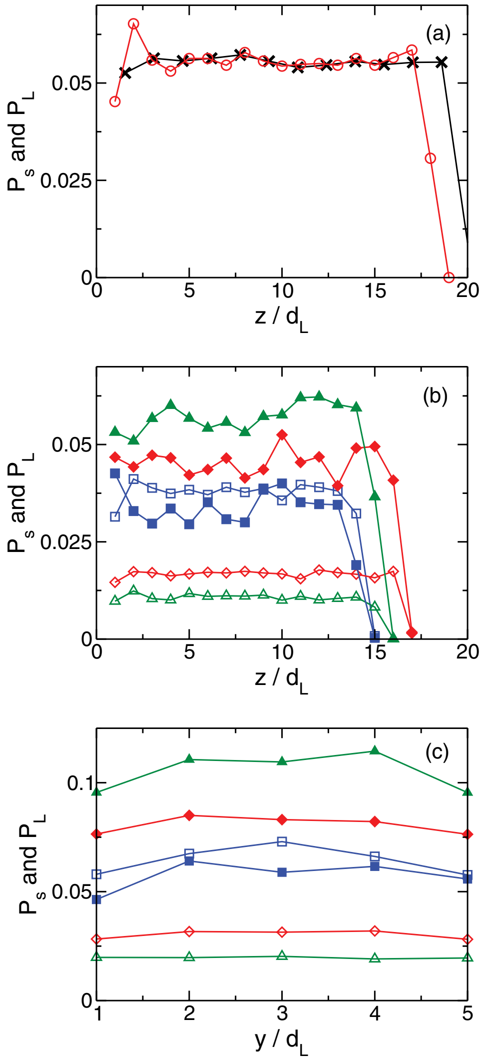

FIG. 5. (Color online) (a) Homogeneity of MSP (○) and MPP (×) along the z axis, expressed as the ratio of the number of grains to the total number of grains in d_L-thick layers. (b) Homogeneity of BSP along the z axis, expressed as the ratio of the number of large (empty symbols) and small (solid symbols) grains to the total number of grains in d_L-thick layers for $x_s = 10\%$ (□), $x_s = 25\%$ (◇), and $x_s = 40\%$ (△). (c) Homogeneity of BSP along the y axis (same calculation method and same key). For (a)–(c), the gap between sidewalls is $W = 5d_L$ and the data have been averaged over three simulations.

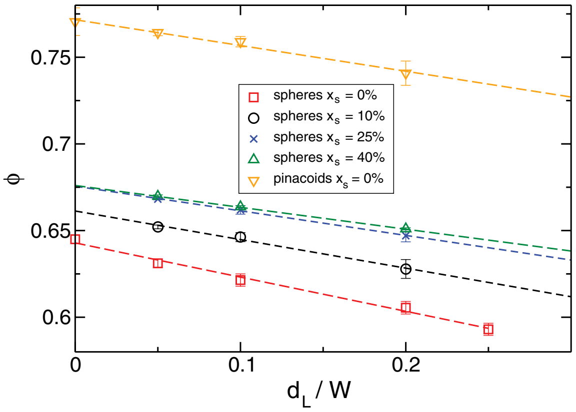

FIG. 6. (Color online) Plot of the average solid fraction versus d_L/W for MSP, BSP, and MPP. The lines are fits from the geometrical model [Eq. (1)]. Error bars denote the standard deviation.

case, small grains partially fill the porosity of the monosized packing and increase the solid fraction. The second limit case corresponds to a packing of small grains to which we add a few large particles ($x_s \approx 100\%$). The largest particles can then be considered as islands in a sea of small grains whose solid fraction is equal to that of a monosized packing: ϕ_{mono}. Since the solid fraction of the islands is equal to 1, the average packing fraction is greater than ϕ_{mono}.

More interestingly, an excellent agreement between our data and the geometrical model is found. The corresponding values of C and ϕ_{bulk} are reported in Table IV. It should be pointed out that the value of ϕ_{bulk} obtained for MSP is consistent with that of the random close packing (0.64) reported in the literature [54].

Note that in Ref. [18], Desmond and Weeks compare the geometrical model with simulations of bidisperse sphere packing (50-50 binary mixture with particle size ratio of 1.4) in the absence of gravity. Our results show that the validity of this model is much broader since it still holds in the presence of gravity for monodisperse sphere packings, for bidisperse sphere packings (independently of the fraction of small grains), as well as for monodisperse pinacoid packings. This result is important in the framework of real granular materials whose grains are far from being perfect spheres. Let us recall that the fit parameter C is equal to $2h(\phi_{\text{bulk}} - \phi_{\text{BL}})$ (see Sec. I). Our results show that when the fraction of small grains, x_s, increases, C decreases. This can be the consequence of a decrease of the distance of propagation of the sidewall effects h and/or of the difference $\phi_{\text{Bulk}} - \phi_{\text{BL}}$. To address this point we will study the local variation of the solid fraction close to the sidewalls. This is the objective of next subsection.

B. Solid fraction profiles

Figure 7 depicts the solid fraction profile as a function of the distance y/d_L to the left sidewall for MSP [Fig. 7(a)], BSP [Fig. 7(b)], and MPP [Fig. 7(c)]. The local solid fraction fluctuates with the distance from the wall, especially in the neighborhood of sidewalls and, if W is large enough, it reaches a uniform value away from the sidewalls. The inset of Fig. 7(a) reports the packing fraction fluctuations as a function of the nondimensional distance from the wall y/d_L. The aforementioned fluctuations clearly reflect the layering due to the presence of sidewalls, i.e., an order propagation in the

TABLE IV. Values of C and ϕ_{bulk} obtained by fitting the data reported in Fig. 6 with Eq. (1).

	Spheres				Pinacoids
x_s	0%	10%	25%	40%	0%
C/d_L	0.197	0.165	0.142	0.126	0.149
Φ_{bulk}	0.643	0.661	0.676	0.676	0.772

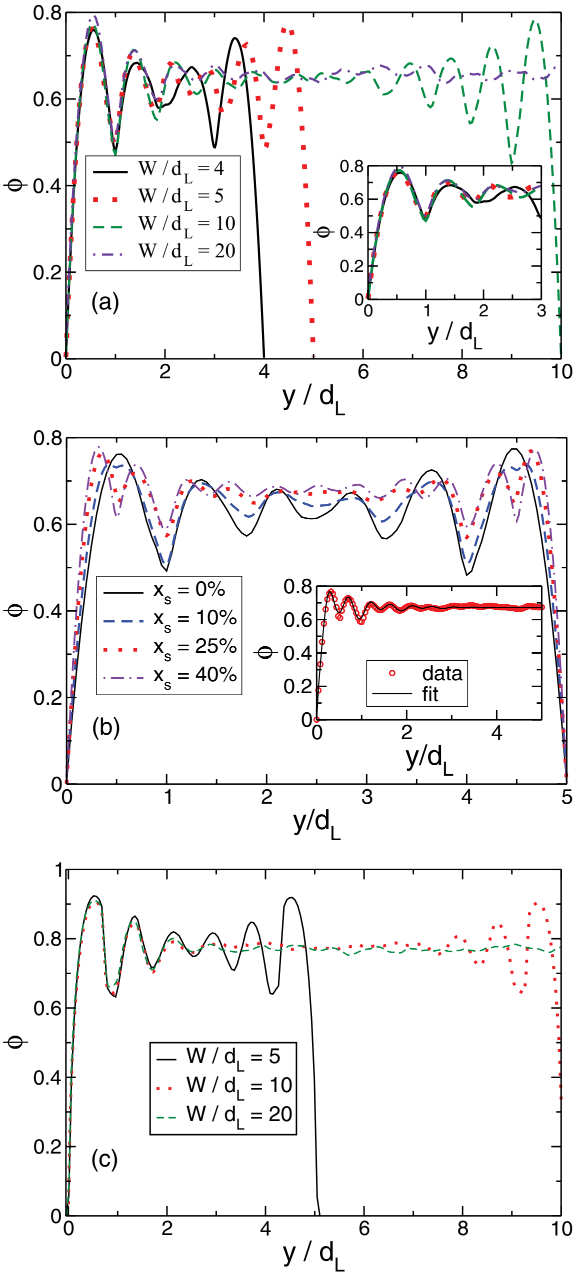

FIG. 7. (Color online) Solid fraction profiles as a function of distance y/d_L from the confining wall for (a) MSP with $W = 4d_L$, $W = 5d_L$, $W = 10d_L$, and $W = 20d_L$; (b) BSP with $W = 5d_L$ and $x_s = 0, 10, 25$, and 40%; and (c) MPP with $W = 5d_L$, $W = 10d_L$, and $W = 20d_L$. Fluctuations of the local solid fraction are due to the layering of particles in the vicinity of the sidewalls. The inset in Fig. 7(a) is a zoom over $3d_L$. The inset in Fig. 7(b) shows the solid fraction for BSP (here $x_s = 40\%$) and the corresponding fit [Eq. (8)].

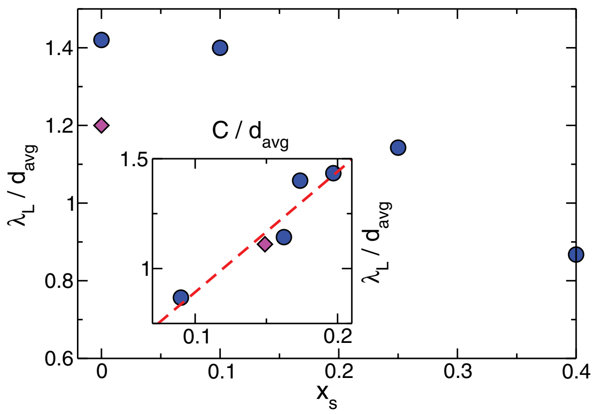

FIG. 8. (Color online) Characteristic length of confinement effect λ_L versus fraction of small grains x_s for MSP and BSP (circle) as well as for MPP (diamond) with $W = 10d$. That length is defined in Eq. (8). The effect of confinement is found to decrease with increasing grain polydispersity or grain angularity. The inset reports the same length versus that of the fit parameter in Eq. (1): $C = 2h(\phi_{\text{bulk}} - \Phi_{\text{BL}})$. The dashed line corresponds to a linear fit.

y direction [11]. For MSP, the confinement effect propagates over approximately $3d_L$ to $4d_L$. As a result, packings for which $W < 6d_L$ to $8d_L$ are influenced by the presence of walls over their full width. In other words, for such size, the order generated by the sidewalls propagates in the whole packing. On the contrary for BSP as well as for MPP, the propagation seems to be shorter (approximately $1.5d_L$ to $2d_L$ for BSP and about $2d_L$ for MPP). The presence of bidispersity or nonsphericity induces disorder in the vicinity of the sidewalls which mitigates the layering. To quantify more precisely the sidewall effects, we have fitted the solid fraction profiles reported in Fig. 7 by the following empirical law:

$$\phi(y) = \left[1-\exp\left(-\frac{y}{\alpha}\right)\right]\left\{\phi_{\text{bulk}} + \sum_{i\in\{S,L\}} \beta_i \cos\left[\frac{\pi(2y-1)}{\gamma_i}\right]\exp\left(-\frac{y}{\lambda_i}\right)\right\}. \quad (8)$$

In this expression, the characteristic lengths of the sidewall effect propagation for large (L) and small (S) grains are respectively λ_L and λ_S. Parameter α characterizes the solid fraction increase close to the sidewalls, and γ_i and β_i respectively correspond to the period and amplitude of the structuration oscillations caused to the solid fraction profile by the layering of small and large particles. For monosized packings, we use the aforementioned fit with $\beta_S = 0$. An example of the obtained fits is plotted in the inset of Fig. 7(b). Let us stress that the fit used is purely empirical. Our aim is to obtain a reasonable approximation for confinement effect propagation rather than a precise description of the solid fraction profiles by an equation.

The values of λ_L (those of λ_S are not statistically relevant for $x_S < 0.25$), normalized by the average grain size d_{avg}, obtained this way are reported in Fig. 8 for $W = 10d_L$. For sphere packings, the normalized characteristic length is found to decrease when the fraction of small spheres x_s increases. Indeed, for $x_s = 0$, we have $\lambda_L/d_{\text{avg}} \approx 1.4$, whereas $\lambda_L/d_{\text{avg}} \approx 0.85$ for $x_s = 40\%$. This decrease proves that the polydispersity mitigates the confinement effect. Moreover, the fact that λ_L/d_{avg} decreases with x_s demonstrates that λ_L decreases quicker than the mean grain size. For MPP we obtain $\lambda/d_{\text{avg}} = 1.2$, which is smaller than the value obtained for MSP. This indicates that the sidewall effect is also mitigated by an increase in grain angularity. Hence, characteristic length

λ_L is expected to correlate with the thickness h of the boundary layers introduced in Eq. (1). In the inset of Fig. 8 we report λ_L versus $C = 2h(\phi_{\mathrm{bulk}} - \phi_{\mathrm{BL}})$ and observe a good linear correlation between these two parameters. Furthermore, the data for both sphere and pinacoid packings collapse on the same straight line whose intercept is equal to zero.

C. Effect of grain-wall friction

So far, the presented simulations were performed with frictionless grains and sidewalls. However, additional simulations were performed to investigate the influence of grain-wall friction. For this purpose, the friction coefficient between grains was kept equal to zero, whereas the grain-wall friction coefficient μ_{gw} was successively set to 0.3, 0.5, and 1. As before, three grain packings were simulated for each grain-wall friction coefficient in order to average the measured quantities. Our aim is not to address this point but just to mention that, in our contact dynamic simulations, we found that the grain-wall friction had no effect since neither the average solid fraction nor the solid fraction profiles were affected by μ_{gw}. This result demonstrates that the influence of confinement on packing fraction is purely geometrical.

V. PACKING MICROSTRUCTURE

Section III established that our packings are homogeneous and that they have reached a stable equilibrium with acceptable interpenetration. Then, in Sec. IV, we verified that the simulated compaction method allows to accurately achieve the 0.64 solid fraction characteristic of the random close-packed state of monodisperse sphere packings when PBC are substituted for sidewalls. Moreover, this method is sufficiently repeatable to show significant influence of the confinement on the solid fraction of various grain packings. Now, Sec. V focuses on the internal state of our packings in order to investigate the influence of confinement on their microstructure. We first investigate the presence of textural order (Sec. V A). Then we study a usual characteristic to describe the microstructure of grain packings: the mean number of contacts per grains (coordination number). For various grain shapes and polydispersities, Sec. V B discusses the influence of confinement on that characteristic.

A. Order

In this section, our aim is to investigate the presence of long-range textural order in the packings. Let us point out here that by long-range order we mean an order that extends to the system size when this size tends towards infinity [55].

In a granular packing, textural order may take various forms [56]: translational arrangements of grains that combine to form patterns, preferential orientation of the contact network, and preferential orientation of nonspherical grains themselves. Each of these aspects is addressed in the following paragraphs.

First, translational arrangements are studied by means of the pair correlation function $g(r)$ [1]. This function is depicted in Fig. 9 for MSP [Fig. 9(a)] and MPP packings [Fig. 9(b)] and for several values of W. For both packings, local order extends over a few particle diameters, slightly less for MPP than for MSP due to the higher angularity of the former, resulting in a loss of rotational symmetry. As a consequence, very confined packings exhibit ordering over their full size. However, for lower confinement (e.g., when $W/d_L = 10$ or more), $g(r)$ tends towards 1 when r increases beyond $3d_L$, indicating the absence of translational long-range ordering within our packings.

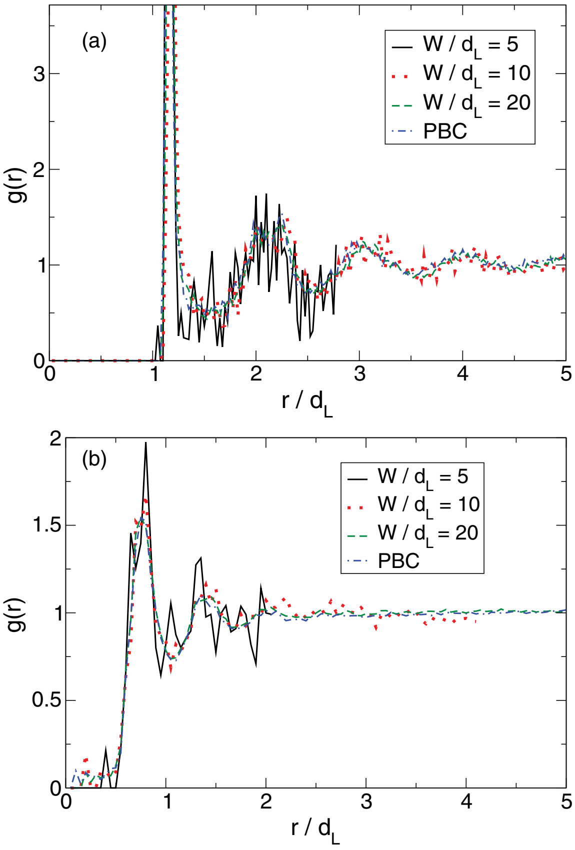

FIG. 9. (Color online) Pair correlation functions of MSP (a) and MPP (b) for several values of W/d_L. These exhibit local order that is stronger for MSP compared to MPP. When r/d_L is large enough, $g(r)$ tends towards 1, indicating the absence of long-range translational order.

Next, the existence of preferential orientations of the contact network is investigated. For this purpose, Fig. 10 displays for various confinements 2D representations of the distributions of contact orientations in MSP away from the bottom plane and the free surface. Given the sidewall-induced layering evidenced in the h-thick boundary layers (see Sec. IV B), contact from the boundary layers [Fig. 10(a)] have been dealt with separately from those located in the bulk region [Fig. 10(b)]. Note that no bulk region is present in monodisperse packings where $W/d_L = 5$ and, conversely, no boundary layer occurs in PBC packings. Furthermore, inside the boundary layers [see Fig. 10(a)], an anisotropy of contact orientations is visible regardless of the confinement in the x, y, and z directions, as well as at roughly 60° to the x direction in the xy plane and 30° to the y direction in the yz plane (corresponding to compact clusters of three spheres close to the sidewalls). This anisotropy is fully consistent with the vertical layering of monodisperse packings close to the sidewalls, with a larger peak in the y direction due to the high proportion of

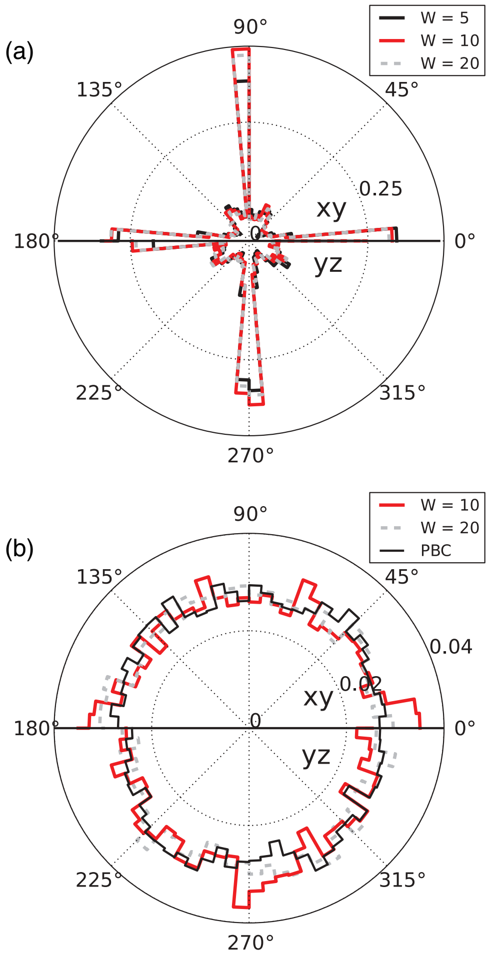

FIG. 10. (Color online) Contact normal orientation distributions for MSP inside the boundary layers (a) and inside the bulk region (b). The upper half of each chart (e.g., from 0° to 180°) corresponds to the xy plane, while lower half corresponds to the yz plane. Several gap widths are considered.

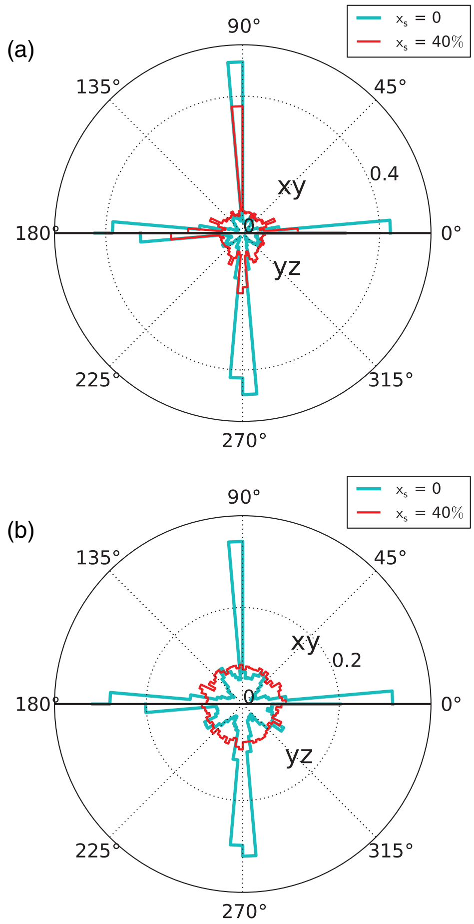

FIG. 11. (Color online) Contact normal orientation distributions for MSP ($x_S = 0$) and BSP ($x_S = 40\%$) inside the boundary layers/closer than $1.5d_L$ to a sidewall (a) and inside the bulk region (b). The upper half of each chart (e.g., from 0 to 180°) corresponds to the xy plane, while lower half corresponds to the yz plane. The gap width is $W = 5d_L$ and the bulk region coincides with particles located at least $1.5d_L$ away from the sidewalls.

sidewall-sphere contacts. Unsurprisingly, in the bulk region, Fig. 10(b) shows that the distribution of contact orientations remains isotropic for all these confinements. In order to assess the effect of polydispersity on the existence of preferential orientations of the contact network, 2D representations of the distributions of contact orientations are depicted in Fig. 11 for $W = 5d_L$-thick packings, away from bottom plane and free surface. Observe that the substitution of $x_S = 40\%$ by mass of small particles for large ones results in the emergence of a central $2d_L$-thick quasi-isotropic bulk region [see Fig. 11(b)]. Furthermore, note that the boundary layers remain anisotropic [see Fig. 11(a)], although the presence of small particles between large ones tends to disturb the vertical layering of the latter (because the centers of inertia of small particles are not necessarily coplanar with those of large particles). Hence, the anisotropy along the axes x, y, and z is mitigated, while other preferential orientations corresponding to various patterns made of small and large grains each in contact with the others are generated. Eventually, in order to assess the effect of grain shape on the existence of preferential orientations of the contact network, 2D representations of the distributions of contact orientations in MPP away from the bottom plane and the free surface are represented in Fig. 12 for various confinements. As for sphere packings, contacts located in boundary layers have been dealt with separately from those located in the bulk region. Inside the boundary layers, an anisotropy of contact orientations is visible regardless of the confinement in the x, y, and z directions [see Fig. 12(a)], and this anisotropy may be explained by the wall-induced layering just like for sphere packings. In the bulk region, Fig. 12(b) shows that pinacoid packings exhibit isotropic contact orientation distributions in the xy plane but not along the z axis where, unlike for sphere packings, some anisotropy is visible even for packings with PBC. This anisotropy may be explained by the deposition under gravity protocol, with pinacoids rotating around their center of inertia under steric hindrance contraints in order to minimize their potential energy.

The anisotropy observed in Figs. 11(b) and 12(b), respectively, for BSP with $x_S = 40\%$ and MPP with PBC, may be calculated and compared to that of the isotropic reference state depicted in Fig. 10(b) with PBC. Given the rotational symmetry of the contact normal orientation distributions in the xy plane [see Figs. 10(b), 11(b), and 12(b)], the anisotropy may

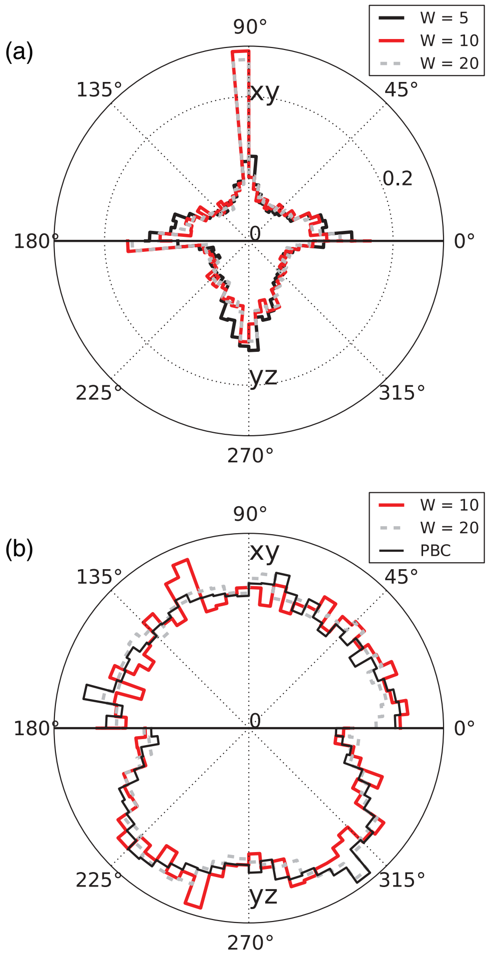

FIG. 12. (Color online) Contact normal orientation distributions for MPP inside the boundary layers (a) and inside the bulk region (b). The upper half of each chart (e.g., from 0° to 180°) corresponds to the xy plane, while the lower half corresponds to the yz plane. Several gap widths are considered.

be quantified using a second-order development of the contact orientation probability density function $P(\vec{n})$ (see Ref. [43] for details),

$$P(\vec{n}) = \frac{1}{4\pi}[1 + a(3\cos^2\theta - 1)], \tag{9}$$

where

(a) $a = 5(F_3 - F_1)/2$ denotes the branch vector coefficient of anisotropy derived from eigenvalues F_3 and F_1 of the fabric tensor [34,43,56] and

(b) θ denotes the polar coordinate in the xy plane.

This coefficient may vary from 0 (perfectly isotropic packing) to 2.5 (perfectly anisotropic packing). Table V gathers values of the branch vector coefficient of anisotropy calculated for MSP with PBC, in the bulk region of BSP with $x_S = 40\%$ and for MPP with PBC. These values show no significant differences between the bulk region of BSP with $x_S = 40\%$ and MSP with PBC. Furthermore, the coefficient of anisotropy of branch vectors obtained for MPP with PBC remains below 0.1, denoting a rather small anisotropy. Last, Fig. 13 shows the distributions of the orientations of simple (face-vertex), double (face-edge), and triple (face-face) contacts, whereby the vertical anisotropy in MPP with PBC is identical no matter the contact type. As a consequence, no long-range contact orientation anisotropy is generated in our frictionless grain packings by the grain deposition protocol used, except a weak anisotropy generated in pinacoid packings along the z axis.

TABLE V. Branch vector coefficient of anisotropy calculated for MSP with PBC ($W/d_L = 20$), in the bulk region of BSP with $x_S =$ 40% ($W/d_L = 5$), and for MPP with PBC ($W/d_L = 20$).

Configuration	MSP (PBC)	BSP ($W/d_L = 5$)	MPP(PBC)
a	0.028 ± 0.011	0.032 ± 0.005	0.081 ± 0.032

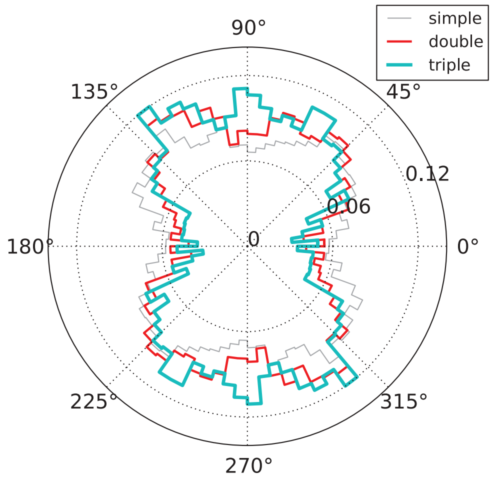

FIG. 13. (Color online) Distribution of the orientations of simple (a), double (b), and triple (c) contacts for MPP in the yz plane. Periodic boundary conditions are used in the x and y directions.

Finally, the orientations of particles that are not symmetric by rotation may also be a source of anisotropy within the packing. To detect a preferential orientation of pinacoids in such a packing, one may use the nematic order parameter Q_{00}^2. Here, we recall briefly how this parameter can be determined (for details, refer to Refs. [57,58]). For each particle, if we call $\vec{u}, \vec{v}, \vec{w}$ the unit vectors of its base of inertia (which, in our case, align with its axes of symmetry) we can define the following tensor [58]:

$$Q_{\alpha\beta}^{uu} = \frac{1}{n}\sum_{i=1}^{n}\left(\frac{3}{2}u_{i\alpha}u_{i\beta} - \frac{1}{2}\delta_{\alpha\beta}\right) \quad \text{with} \quad \alpha,\beta = 1,2,3,$$

where n is the number of particles and δ the Kronecker symbol. We apply the same definition with $Q_{\alpha\beta}^{vv}$ and $Q_{\alpha\beta}^{ww}$. From those tensors, the nematic order parameter can be determined,

$$Q_{00}^2 = {}^t\vec{Z}\, Q^{zz}\vec{Z},$$

where $\vec{Z}$ is the eigenvector corresponding to the larger eigenvalue of the three tensors Q^{uu}, Q^{vv}, and Q^{ww}. Q^{zz} is the corresponding diagonalized tensor. By construction, this parameter varies between 0 and 1. For each of our pinacoid packings, two values of the nematic order parameter have been calculated, one corresponding to particles located in a boundary layer, and one corresponding to particles located in the bulk region. Whatever the confinement, the nematic order parameter ranges between 0.05 and 0.07 in the bulk region,

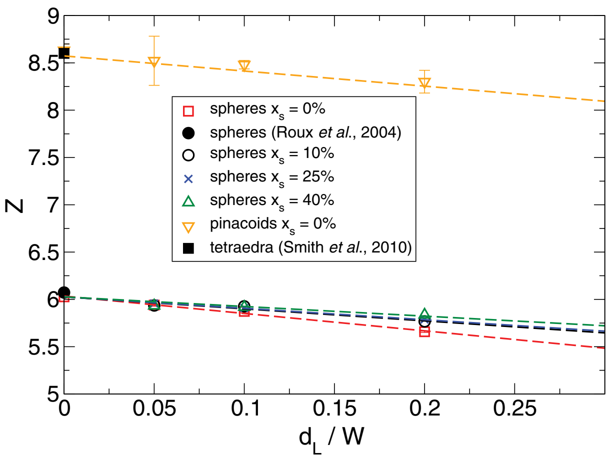

FIG. 14. (Color online) Coordination number as a function of d_L/W for MSP and MPP. Error bars on pinacoid packings results denote the standard deviation (not represented for sphere packings because errors are smaller than symbol size). The linear relationship between Z and d_L/W suggests that the geometrical model, initially derived for the packing fraction, is also valid for the coordination number.

which is quite low and shows the absence of privileged grain orientation, whereas it is slightly higher in the boundary layers (between 0.105 and 0.128).

As a conclusion of this subsection, frictionless grain packings used in the present work do not exhibit significant long-range order, except a weak anisotropy of the contact orientation distributions observed in pinacoid packings along the z axis. Furthermore, sidewalls induce order close to their location that, in the case of very confined packing, propagates over the whole system.

B. Coordination number

Figure 14 shows the variations of the coordination number with d_L/W for MSP, BSP, and MPP. Each value is averaged over three simulations and the error bars denote the corresponding standard deviation. Preliminary examination of our results obtained with biperiodic boundary conditions (unconfined state with $d_L/W \rightarrow 0$) suggests the following remarks: For sphere packings, the calculated coordination number is 6.027 ± 0.012, which is very close to the 6.073 ± 0.004 value calculated by Ref. [48] in the RCP state. For pinacoid packings, the calculated coordination number is 8.581 ± 0.068. Although no study of pinacoid packings could be found in the literature, such a high coordination number value has already been observed in disordered packings of particles having a similar shape (8.6 ± 0.1, calculated by Ref. [59] for packings of tetraedra on extrapolation to the jamming point).

When confinement increases, the coordination number decreases linearly for both MSP and MPP, which is consistent with the linear decrease of the solid fraction evidenced in Fig. 6. Though MPP coordination number values tend to be more scattered than MSP ones, which could be due to a combination of finite-packing-size effects with the higher level of interpenetration observed in pinacoid packings. Nevertheless, the aforementioned linear relation between Z and $1/W$ suggests a generalization of the geometrical model to the coordination number. For this purpose, let us define Z_{bulk} and Z_{BL}, respectively, the coordination number for the bulk region and the coordination number for the boundary layers. By writing the coordination number as the average of Z_{bulk} and Z_{BL} weighted by the thicknesses of their respective zones (respectively, $W - 2h_Z$ and $2h_Z$), we obtain

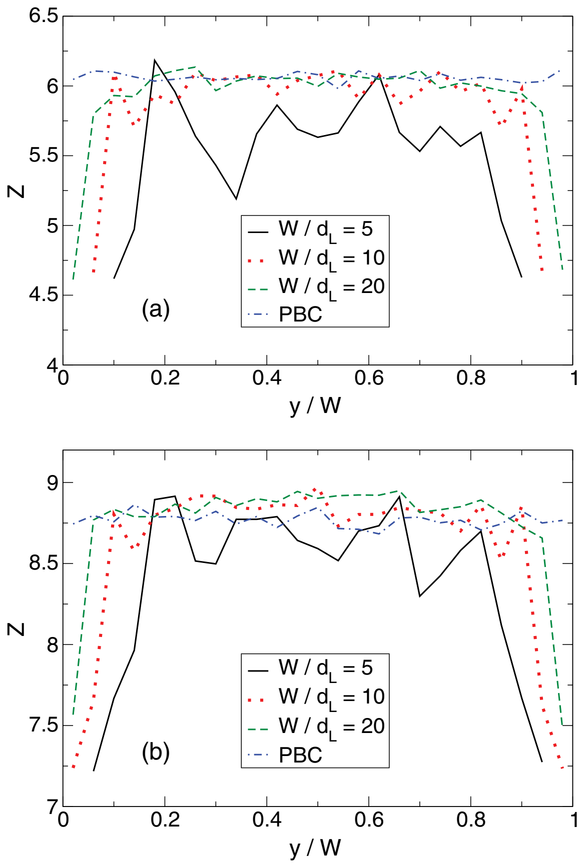

FIG. 15. (Color online) Coordination number profiles (along y) for MSP (a) and for MPP (b) for several gap width. These profiles evidence a constant central zone and two drop zones in contact with the sidewalls.

$$Z = \frac{W - 2h_Z}{W} Z_{\mathrm{bulk}} + \frac{2h_Z}{W} Z_{\mathrm{BL}} = Z_{\mathrm{bulk}} - \frac{C_Z}{W}, \qquad (10)$$

with $C_Z = 2h_Z(Z_{\mathrm{bulk}} - Z_{\mathrm{BL}})$.

Figure 14 also shows that the influence of polydispersity on packing coordination number Z decreases to zero when the confinement diminishes, which is consistent with Ref. [60]. Indeed, in the unconfined state, the lack of contacts of small spheres with others (due to the steric hindrance of large ones) is compensated by the excess of contacts of large spheres with small ones.

To investigate the coordination number decrease with increasing confinement, Fig. 15 depicts coordination number profiles in the y direction (normal to the sidewalls) for sphere and for pinacoid packings. Each of these profiles is averaged over three simulations and is determined on subdividing the packing into slices perpendicular to the y direction and calculating for each slice the average number of contacts per particle having its center of inertia in the slice. In confined state, all these profiles evidence a central zone where the coordination number is almost unchanged compared to the unconfined reference state (except for sphere packings with $W = 5d_L$) and two "drop zones" in contact with the sidewalls where the coordination number symmetrically drops by 1.4 (for sphere packings) to 1.5 contacts (for pinacoid packings) from their respective unconfined reference state. The thicknesses of these drop zones look identical to that of the boundary layers described in the geometrical model [18], leading to the same conclusion that grain angularity mitigates the effect of sidewalls on the coordination number drop in their vicinity.

To confirm this observation, we may consider the geometrical model and compare $\zeta_\phi = C/\phi_{\text{bulk}}$ with $\zeta_Z = C_Z/Z_{\text{bulk}}$. For MSP, we obtain $\zeta_\phi = 0.304$ and $\zeta_Z = 0.305$ and for MPP $\zeta_\phi = 0.186$ and $\zeta_Z = 0.193$. Note that the values of ζ_ϕ and ζ_Z are also comparable in the case of BSP. The strong correlation between those two quantities shows that the propagation of the confinement effect is comparable for the two studied quantities: ϕ and Z. As described in Sec. II D, pinacoid packings incorporate simple, double, and triple contacts and it is of interest to investigate the effect of confinement on their respective distribution. Therefore, Fig. 16 depicts the coordination number profiles of MPP for simple [Fig. 16(a)], double [Fig. 16(b)], and triple contacts [Fig. 16(c)]. Like in Fig. 15, all these profiles evidence a central zone where coordination number values are almost unchanged compared to the unconfined reference state (except for sphere packings with $W = 5d_L$). These values are $Z_s \approx 5$, $Z_d \approx 1.7$, and $Z_t \approx 1.8$, respectively, for simple, double, and triple contacts.

In order to check the relevance of these coordination number values, one shall observe that packings of n frictionless rigid grains at equilibrium obey the following relation [49] among the degree of hypostaticity k_0, the degree of hyperstaticity h_0, the number of contacts that carry forces $N_c = \frac{n}{2}(Z_s + 2Z_d + 3Z_t)$, and the number of degrees of freedom $N_f = 6n$ of the packing:

$$\begin{aligned} N_f + h_0 = N_c + k_0 \Leftrightarrow 12 + 2\frac{h_0}{n} \\ = Z_s + 2Z_d + 3Z_t + 2\frac{k_0}{n}. \end{aligned} \quad (11)$$

If we assume that the pinacoids in our packings are randomly oriented, which seems reasonable according to the values of the nematic order parameter (see Sec. V A), then no motion is possible without generating work in the contacts network, which means that the degree of indeterminacy of contact forces in the packing is zero; therefore, k_0 should be set to 0 in Eq. (11). On incorporating in Eq. (11) the aforementioned coordination number values as well as that of k_0, one obtains

$$2\frac{h_0}{n} = 13.8 - 12 = 1.8. \quad (12)$$

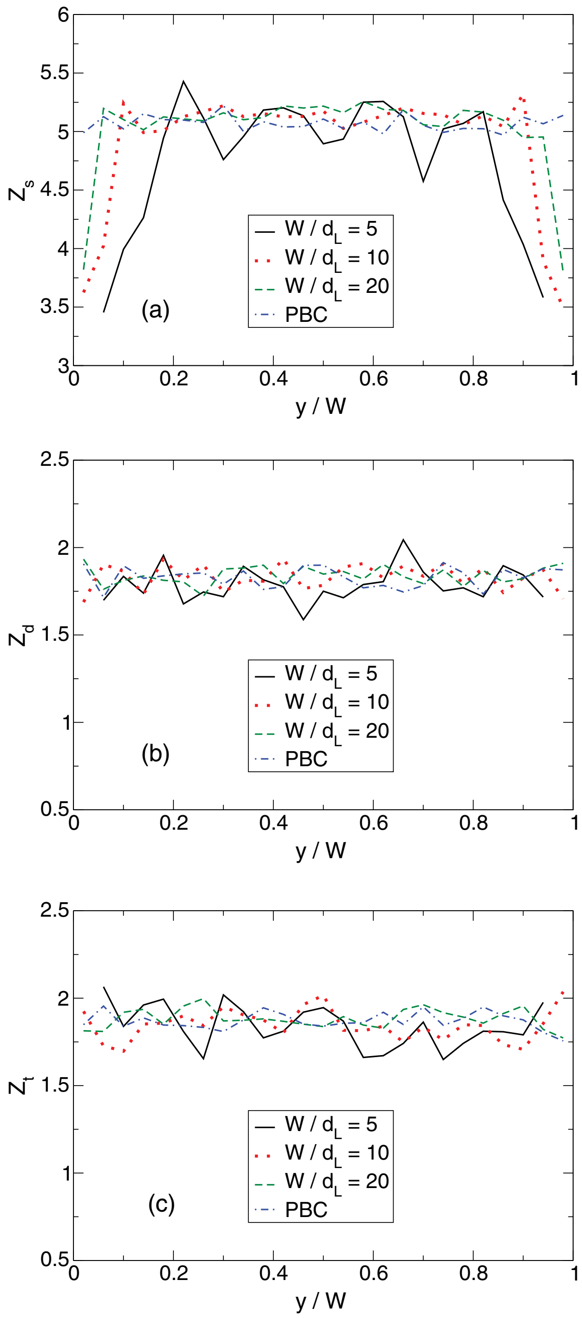

FIG. 16. (Color online) Coordination number profiles (along y) of MPP for simple (a), double (b), and triple contacts (c) for confined ($W \in [5d_L, 20d_L]$) and unconfined packings.

Observe that, for isostatic pinacoid packings (e.g., $h_0 = 0$), Eq. (11) would lead to $Z_s + 2Z_d + 3Z_t = 12$. Here, it is clear that $Z_s + 2Z_d + 3Z_t > 12$. The level of interpenetretation calculated in Sec. III B together with the finite size of packings may lead to a sum $Z_s + 2Z_d + 3Z_t$ slightly higher that 12, but it is doubtful that this sum would reach 13.8 on this sole explanation. The presence of hyperstaticity in our pinacoid packings seems more realistic and at least consistent with Eq. (12) and with our finding of as much as 2 triple contacts per grain ($Z_t \approx 1.8$). Although interesting, further investigation of the presence of hyperstaticity falls beyond the scope of the present paper.

Coming back to Fig. 16, the profiles show that MPP exhibit more simple contacts than the sum of double and triple contacts. They also evidence that confinement primarily affects the simple contact profiles, whereas double and triple contact profiles remain unchanged. As a consequence, the vicinity of sidewalls is not a privileged location for edge-to-face or

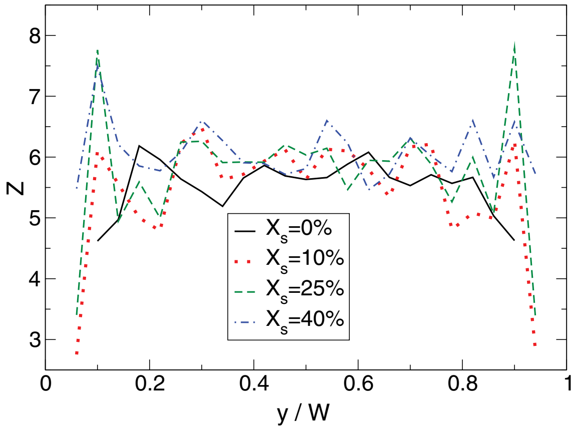

FIG. 17. (Color online) Coordination number profiles (with y) for BSP. The gap between sidewalls is $W = 5d_L$.

face-to-face contacts, although a drop in the simple contact profiles tends to make them look over-represented.

For a fixed confinement, Fig. 17 shows the influence of polydispersity on coordination number profiles in the y direction (normal to the sidewalls) for sphere packings. As before, each of these profiles is averaged over three simulations and is determined on slicing the packing perpendicular to the y direction. As observed in Fig. 7(b), an increasing polydispersity does not seem to impact the bulk region but rather reduces the thickness of the boundary layers and, hence, mitigates the effect of sidewalls confinement on the coordination number.

Finally, like for the solid fraction, we have not observed any effect of the grain-wall friction coefficient on the coordination number of MSP.

VI. CONCLUSION

In this work, we have shown how a confining boundary alters the solid fraction as well as the internal structure of static frictionless granular materials compacted under their own weight using the nonsmooth contact dynamics simulation method. We did not restrict ourselves to sphere packings but extended our work to packings made of a particular type of polyhedra: pinacoids.

As previously reported, the presence of sidewalls induces short-range order in their vicinity. Except for a weak contact orientation anisotropy observed with pinacoid packings in the vertical direction, no long-range order was observed in our packings. We have demonstrated that both the polydispersity and the angularity of grains lower the confinement effect. This effect has been observed for the solid fraction and for the coordination number. Our results have shown that the geometrical model [18–21] that captures the linear evolution of the solid fraction versus $-1/W$ is valid for sphere packings as well as for pinacoid packings and that it holds whatever the packing polydispersity.

Interestingly, this model, initially derived for the packing fraction, can be extended to capture the effect of confinement on the coordination number. The characteristic length quantifying the effect of the sidewalls is found to be the same for those two quantities.

Finally, we have shown that the effect of wall friction is negligible, indicating that the major influence of the confining sidewalls is geometric.

Several perspectives arise from this study, among which the need to address with more details the presence of hyperstaticity in our packings of frictionless pinacoids.

ACKNOWLEDGMENTS

We thank F. Chevoir, J.-N. Roux, G. Saussine, N. Roquet, and N. N. Medvedev for helpful conversations. Many thanks to the LMGC90 team in Montpellier for making their simulation platform freely available. We are also grateful to O. Garcin for technical support.

---

[1] L. E. Silbert, D. Ertaş, G. S. Grest, T. C. Halsey, and D. Levine, Phys. Rev. E **65**, 031304 (2002).

[2] I. Agnolin and J.-N. Roux, Phys. Rev. E **76**, 061302 (2007).

[3] N. Taberlet, P. Richard, A. Valance, W. Losert, J.-M. Pasini, J. T. Jenkins, and R. Delannay, Phys. Rev. Lett. **91**, 264301 (2003).

[4] N. Taberlet, P. Richard, E. Henry, and R. Delannay, Europhys. Lett. **68**, 515 (2004).

[5] P. Jop, Y. Forterre, and O. Pouliquen, J. Fluid Mech. **541**, 167 (2005).

[6] N. Taberlet, P. Richard, and J. E. Hinch, Phys. Rev. E **73**, 050301 (2006).

[7] P. Richard, A. Valance, J.-F. Métayer, P. Sanchez, J. Crassous, M. Louge, and R. Delannay, Phys. Rev. Lett. **101**, 248002 (2008).

[8] N. Taberlet, P. Richard, and R. Delannay, Comput. Math. Appl. **55**, 230 (2008).

[9] G. Pereira, M. Sinnott, P. Cleary, Kurt Liffman, Guy Metcalfe, and Ilija Sutalo, Granul. Matter **13**, 53 (2011).

[10] R. Ben Aim and P. le Goff, Powder Technol. **2**, 1 (1968).

[11] M. Suzuki, T. Shinmura, K. Iimura, and M. Hirota, Adv. Powder Technol. **19**, 183 (2008).

[12] J. W. Landry, G. S. Grest, L. E. Silbert, and S. J. Plimpton, Phys. Rev. E **67**, 041303 (2003).

[13] J. W. Landry, G. S. Grest, and S. J. Plimpton, Powder Technol. **139**, 233 (2004).

[14] A. Seguin, Y. Bertho, and P. Gondret, Phys. Rev. E **78**, 010301 (2008).

[15] L. Vanel, P. Claudin, J. P. Bouchaud, M. E. Cates, E. Clement, and J. P. Wittmer, Phys. Rev. Lett. **84**, 1439 (2000).

[16] C. H. Liu, H. M. Jaeger, and S. R. Nagel, Phys. Rev. A **43**, 7091 (1991).

[17] S. Courrech du Pont, P. Gondret, B. Perrin, and M. Rabaud, Europhys. Lett. **61**, 492 (2003).

[18] K. W. Desmond and E. R. Weeks, Phys. Rev. E **80**, 051305 (2009).

[19] L. C. Verman and S. Banerjee, Nature **157**, 584 (1946).

[20] R. L. Brown and P. G. W. Hawksley, Nature (London) **157**, 585 (1946).

[21] G. Combe, Ph.D. thesis, École Nationale des Ponts et Chaussées, 2001, http://gael.combe.pagesperso-orange.fr/these.pdf.

[22] A. P. F. Atman, P. Brunet, J. Geng, G. Reydellet, G. Combe, P. Claudin, R. P. Behringer, and E. Clément, J. Phys.: Condens. Matter **17**, S2391 (2005).

[23] P. Ribière, P. Richard, R. Delannay, and D. Bideau, Phys. Rev. E **71**, 011304 (2005).

[24] P. Ribière, P. Richard, D. Bideau, and R. Delannay, Eur. Phys. J. E **16**, 415 (2005).

[25] K. Szarf, G. Combe, and P. Villard, Powder Technol. **208**, 279 (2011).

[26] C. Tourenq and A. Denis, *Les Essais de Granulats* (Rapport de Recherche du Laboratoire Central des Ponts et Chaussées, Paris, 1982), Vol. 114.

[27] C. Murray, MRS Bul. **23**, 33 (1998).

[28] Lee-Wen Teng, Pei-Shan Tu, and Lin I, Phys. Rev. Lett. **90**, 245004 (2003).

[29] R. Laniel, Ph.D. thesis, Université de Montpellier 2, 2007, http://perso.univ-rennes1.fr/romain.laniel/memoire_these.pdf.

[30] J. J. Moreau, Eur. J. Mech. A/Solids **13**, 93 (1994).

[31] J.-J. Moreau and M. Jean, Eng. Sys. Design Anal. **4**, 201 (1996).

[32] M. Jean, Comput. Methods Appl. Mech. Eng. **177**, 235 (1999).

[33] F. Dubois and M. Jean, In *Actes du sixième colloque national en calcul des structures*, CSMA-AFM-LMS, Vol. 1, pp. 111–118, (Ecole Polytechnique, Palaiseau, France, 2003).

[34] F. Radjaï and F. Dubois (eds.), *Discrete Numerical Modeling of Granular Materials* (Wiley, New York, 2011).

[35] E. Azéma, F. Radjaï, R. Peyroux, and G. Saussine, Phys. Rev. E **76**, 011301 (2007).

[36] G. Saussine, C. Cholet, P. E. Gautier, F. Dubois, C. Bohatier, and J-J. Moreau, Comput. Methods Appl. Mech. Eng. **195**, 2841 (2006).

[37] F. Chevoir, M. Prochnow, J. T. Jenkins, and P. Mills, in *Powders and Grains 2001*, edited by Y. Kishino (Balkema, Rotterdam, 2001), pp. 373–376.

[38] G. Lois, A. Lemaître, and J. M. Carlson, Phys. Rev. E **72**, 051303 (2005).

[39] G. Lois, A. Lemaître, and J. M. Carlson, Europhys. Lett. **76**, 318 (2006).

[40] E. Azéma, F. Radjaï, R. Peyroux, F. Dubois, and G. Saussine, Phys. Rev. E **74**, 031302 (2006).

[41] N. Estrada, A. Taboada, and F. Radjaï, Phys. Rev. E **78**, 021301 (2008).

[42] E. Azéma, F. Radjaï, R. Peyroux, V. Richefeu, and G. Saussine, Eur. Phys. J. E **26**, 327 (2008).

[43] E. Azéma, F. Radjai, and G. Saussine, Mech. Mater. **41**, 729 (2009).

[44] E. Azéma and F. Radjaï, Phys. Rev. E **81**, 051304 (2010).

[45] J. C. Macrae and W. A. Gray, Br. J. Appl. Phys. **12**, 164 (1961).

[46] S. Emam, J.-N. Roux, J. Canou, A. Corfdir, and J. C. Dupla, in *Powder and Grains 2005* (Balkema, Rotterdam, 2005).

[47] Z. P. Zhang, L. F. Liu, Y. D. Yuan, and A. B. Yu, Powder Technol. **116**, 23 (2001).

[48] J.-N. Roux, arXiv:cond-mat/0405358v1 (2004).

[49] J.-N. Roux, Phys. Rev. E **61**, 6802 (2000).

[50] B. Smit and D. Frenkel, *Understanding Molecular Simulation: From Algorithms to Applications* (Academic Press, San Diego, 2001).

[51] G. Saussine, Ph.D. thesis, Université de Montpellier 2, 2004, http://tel.archives-ouvertes.fr/index.php?halsid=d3ffi3asbs0trqdah142utbmh7&view_this_doc=tel-00077519&version=1.

[52] P. Richard, A. A. Gervois, L. Oger, and J.-P. Troadec, Europhys. Lett. **48**, 415 (1999).

[53] P. Richard, L. Oger, J. P. Troadec, and A. Gervois, Eur. Phys. J. E **6**, 295 (2001).

[54] S. Torquato, T. M. Truskett, and P. G. Debenedetti, Phys. Rev. Lett. **84**, 2064 (2000).

[55] A. Ricci, P. Nielaba, S. Sengupta, and K. Binder, Phys. Rev. E **74**, 010404 (2006).

[56] B. Cambou, M. Jean, and F. Radjaï (eds.), *Micromechanics of Granular Materials* (ISTE, London, UK, 2010).

[57] P. J. Camp and M. P. Allen, J. Chem. Phys. **106**, 6681 (1997).

[58] B. S. John, A. Stroock, and F. A. Escobedo, J. Chem. Phys. **120**, 9383 (2004).

[59] K. C. Smith, M. Alam, and T. S. Fisher, Phys. Rev. E **82**, 051304 (2010).

[60] J.-N. Roux, F. Chevoir et F. Toussaint, Bulletin des Laboratoires des Ponts et Chaussées **268-269**, 141 (2007).